A&A, 709, A121 (2026)
https://doi.org/10.1051/0004-6361/202659770

Astronomy & Astrophysics

An 18–25 GHz spectroscopic survey of southern hemisphere dense cores

Dariusz C. Lis[1,⋆], Karen Willacy[1], Liton Majumdar[2,3], Jorge L. Pineda[1], Susanna Widicus Weaver[4,5], and Shinji Horiuchi[6]

[1] Jet Propulsion Laboratory, California Institute of Technology, 4800 Oak Drove Drive, Pasadena, CA 91109, USA
[2] Exoplanets and Planetary Formation Group, School of Earth and Planetary Sciences, National Institute of Science Education and Research, Jatni 752050, Odisha, India
[3] Homi Bhabha National Institute, Training School Complex, Anushaktinagar, Mumbai 400094, India
[4] Department of Astronomy, University of Wisconsin-Madison, 475 N Charter St, Madison, WI 53706, USA
[5] Department of Chemistry, University of Wisconsin-Madison, 1101 University Ave, Madison, WI 53706, USA
[6] CSIRO Space & Astronomy/NASA Canberra Deep Space Communication Complex, PO Box 1035, Tuggeranng ACT 2901, Australia

Received 9 March 2026 / Accepted 6 April 2026

ABSTRACT

We extended the radio *K*-band spectroscopic survey for organics in southern hemisphere dense cores by observing seven sources using NASA's Deep Space Network 70 m antenna in Canberra, Australia, over the frequency range 18–25 GHz. Molecular column densities of NH_3, *c*-C_3H_2, HC_3N, HC_5N, CCS, C_3S, and *c*-C_3HD were derived for each source assuming local thermodynamic equilibrium. The resulting column density ratios were compared with predictions of a state-of-the art astrochemical model to constrain the C/O ratio and chemical age of each source. Most cores have similar C/O ratios of 0.5−0.7, much different from the best studied TMC-1 dense core, which is characterized by a high C/O ratio of ∼1.4. The chemical ages of the cores are also similar and fall between 0.6 and 5 Myr. The less dense cores tend to have the oldest chemical ages, as might be expected given that chemical timescales scale with density. Our results showcase the synergistic approach of combining radio observations using the DSS-43 antenna with state-of-the-art astrochemical models to study the chemical composition of southern hemisphere dense cores, enabling constraints to be placed on their C/O ratios and chemical ages, which remain largely unexplored.

Key words. astrochemistry – ISM: abundances – ISM: molecules – radio lines: ISM

1. Introduction

Recent molecular detections of aromatic compounds and a wide range of interstellar complex organic molecules (COMs) in the Taurus Molecular Cloud (TMC-1; see McGuire et al. 2018, 2020; Cernicharo et al. 2022 and references therein) have motivated extensive broadband spectral surveys of this dense cloud. Two prominent examples include the *Q*-Band Ultrasensitive Inspection Journey to the Obscure TMC-1 Environment (QUIJOTE) survey conducted with the Yebes telescope (Cernicharo et al. 2021) and the GBT Observations of TMC-1: Hunting Aromatic Molecules (GOTHAM) survey conducted with the Green Bank Telescope (McGuire et al. 2018). Together, these surveys have revealed an extraordinary molecular richness in TMC-1, uncovering numerous carbon-bearing molecules and highlighting the central role of carbon chemistry in cold interstellar environments.

Carbon forms the backbone of organic molecules, many of which are considered potential precursors to prebiotic species on Earth. For this reason, carbon chemistry plays a fundamental role in chemical pathways that may ultimately lead to habitable planetary environments around other stars (Bergin et al. 2026). The growing inventory of aromatic species detected in TMC-1 further emphasizes this importance. Recent discoveries include CN-substituted derivatives of aromatic molecules such as naphthalene (McGuire et al. 2021), as well as larger aromatic species related to acenaphthylene (Cernicharo et al. 2024), pyrene (Wenzel et al. 2024, 2025a), and coronene (Wenzel et al. 2025b). Polycyclic aromatic hydrocarbons are also thought to represent a major reservoir of interstellar carbon, with approximately 10–25% of the cosmic carbon budget potentially locked in these species (Tielens 2008). These discoveries demonstrate that complex carbon chemistry can proceed efficiently at the very low temperatures characteristic of cold dense cores such as TMC-1.

Despite the remarkable chemical complexity revealed in TMC-1, it remains unclear whether this level of molecular richness is typical of dense cores in general or whether TMC-1 represents a particularly favorable chemical environment. Addressing this question requires systematic surveys of the chemical composition across a broader sample of dense cores. Such studies are essential for identifying the dominant chemical pathways responsible for the formation of key carbon-bearing species, including long carbon-chain molecules and COMs, and for determining how widespread these chemical processes are within interstellar molecular clouds.

Lis et al. (2025) present radio *K*-band (18–25 GHz) observations of two cores in the southern Chamaeleon complex carried out using NASA's Deep Space Network (DSN) 70 m antenna in Canberra, Australia (DSS-43), covering the frequency range 18–25 GHz. They surveyed the Class 0 protostar Cha-MMS1

⋆ Corresponding author: dcl@caltech.edu

Table 1. Coordinates, sizes, and temperatures of the observed cores.

Source	Position	Reference	Distance	Time
HOPS-108	05:35:27.08 –05:10:00.1	05:35:51.23 –05:10:00.1	0.4	28.5
HOPS-373	05:46:30.91 –00:02:35.2	05:46:42.52 –00:07:50.6	0.4	18.4
Vela C IRS 31 14	08:58:11.60 –42:37:33.6	08:57:48.00 –42:33:25.0	0.9	18.7
BHR71-IRS1	12:01:36.50 –65:08:49.4	12:00:58.07 –65:10:46.0	0.2	1.8
G300.91+0.88	12:34:14.26 –61:55:22.7	12:33:51.50 –61:59:35.0	4.4	18.3
G304.76+1.34	13:06:45.73 –61:28:39.9	13:07:31.40 –61:31:00.0	–	6.8
G309.91+0.32	13:50:54.57 –61:44:22.1	13:50:25.00 –61:47:50.0	5.5	4.1

Notes. Entries in the table are source, ON and OFF positions (J2000), distance (in kpc), and on-source observing time (h).

and the pre-stellar core Cha-C2, which represent different evolutionary stages of dense cores. Several molecules were detected, including the carbon-chain species HC_3N, HC_5N, C_4H, CCS, C_3S, c-C_3H_2, c-C_3HD, and NH_3. A longer cyanopolyyne, HC_7N, was also detected with high confidence through spectral stacking analysis. While the molecular column densities in the two Chamaeleon cores are typically an order of magnitude lower than those at the cyanopolyyne peak in TMC-1, the molecular abundance ratios are generally consistent with the values observed in TMC-1. The two exceptions are c-C_3H_2, which is higher by a factor of ∼25 relative to the cyanopolyynes in the Chamaeleon cores, and NH_3, which is higher by a factor of ∼125.

Here, we extend the DSS-43 radio K-band observations to seven additional southern hemisphere dense cores and compare their molecular abundance ratios to state-of-the-art time-dependent chemical models. In Sect. 2 we discuss the DSS-43 observations, in Sect. 3 we derive the properties of the cores and molecular column densities, and in Sect. 4 we compare their chemical composition with model predictions. In Sect. 5 we summarize our results and describe the next steps needed to trace the evolution of prebiotic compounds in dense cores.

2. Deep Space Network observations

The DSN technical capabilities for astrochemistry research have improved significantly in recent years with the installation of a new cryogenic dual-horn dual-polarization 17–27 GHz receiver at the DSS-43 in Canberra, Australia (Kuiper et al. 2019), equipped with a broadband digital spectrometer (Virkler et al. 2020) that has 8 GHz of instantaneous bandwidth, enabling observations of multiple transitions of heavy molecular species. Such observations can be used to characterize the density and temperature of the gas with radiative transfer models and derive dynamical information from the line width and velocity at the line peak. The spectrometer provides sufficiently high spectral resolution (30.5 kHz, or 0.35–0.49 km s^{-1}) to resolve narrow molecular line shapes even in the coldest regions (∼10 K) of dense cores (see Lis et al. 2025). A list of molecular transitions covered by the DSS-43 K-Band receiver is given in Table 1 of Lis et al. (2025), and complete molecular spectroscopy data can be obtained from the Cologne Database for Molecular Spectroscopy (CDMS) catalog Müller et al. (2001, 2005)[1].

The source sample for the present observations includes three sources from the Atacama Large Millimeter/submillimeter Array (ALMA) COMPASS program (ALMA Large Program 2022.1.00316L): HOPS-108, HOPS373, and BHR-71. In addition, we observed Vela C IRS 31 12, and four sources from the deuterated ammonia survey of Wienen et al. (2021) characterized by low kinetic temperatures and high D/H ratios in ammonia: G300.91+0.88, G304.76+1.34, and G309.91+0.32. All targets are easily accessible to DSS-43, without conflicts with deep-space communications, which is the primary objective of the antenna. The source coordinates, including the reference positions used for the DSS-43 position-switched observations, are listed in Table 1. The reference positions were chosen as emission-free regions in the 350 μm dust continuum images from the *Herschel* Spectral and Photometric Imaging Receiver (SPIRE) instrument, downloaded from the European Space Agency (ESA) *Herschel* Science Archive[2]. The SPIRE images were also used to constrain the source size needed for determination of molecular column densities (Sect. 3.3).

All of the targeted sources are embedded protostars or pre-stellar cores. HOPS-108 and HOPS 373 are compact protostars identified as part of the *Herschel* Orion Protostar Survey (Furlan et al. 2016) and also characterized by Very Large Array (VLA) and ALMA observations as having rich chemistry (Tobin et al. 2019). Vela C IRS 31 12 is a class I protostar also displaying rich chemistry as observed in 3 mm observations using Mopra (Saul 2022). The sources G300.91+0.88, G304.76+1.34, and G309.91+0.32 were all identified as embedded protostellar cores in the APEX Telescope Large Area Survey of the Galaxy (ATLAS GAL) program (Urquhart et al. 2017, 2019) and were specifically targeted here because of the previous detections of deuterated ammonia (Wienen et al. 2021).

Several DSS-43 observing runs were carried out between 2024 April and 2025 March. The DSN Canberra K-band digital spectrometer processes sixteen 1-GHz-wide bands, which are split into eight separate bands from 18 to 26 GHz for each polarization (Virkler et al. 2020). Each band consists of 32 768 channels with a 30.5 kHz resolution, corresponding to a velocity resolution of 0.35–0.49 km s^{-1}, depending on the frequency. Typical system temperatures at the elevation of the sources were ∼53–63 K. The total on-source integration times varied between 1.8 and 28 hours (Table 1).

The raw data from the spectrometer were processed into calibrated ON-OFF spectra using the standard DSS-43 data reduction pipeline. The system temperature, continuously monitored using a power meter and scaled with a factor derived using a noise diode and an ambient load before the observation, was used in the standard ON-OFF calibration to obtain spectra in antenna temperature units, T_A^*. We refer the reader to Kuiper et al. (2019) for details on the absolute system and receiver

[1] Accessible online at https://cdms.astro.uni-koeln.de/classic/, from the CLASS Weeds package, or via the Splatalog interface at https://splatalogue.online/

[2] https://archives.esac.esa.int/hsa/whsa/

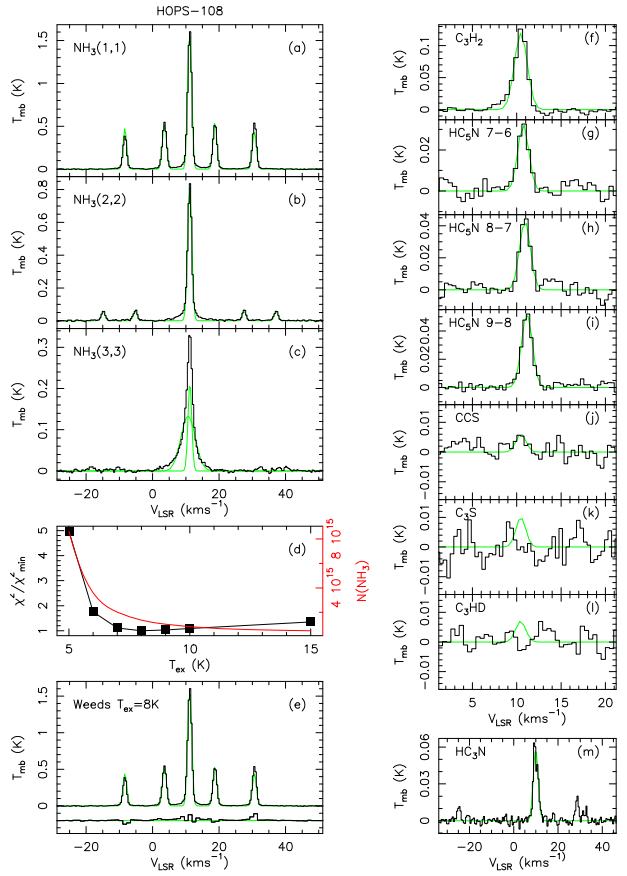

Fig. 1. DSS-43 observations of HOPS-108. Panels a–c: ammonia inversion lines. Green curves correspond to HFS fits to the (1,1) and (2,2) transitions and a two-component Gaussian fit to the (3,3) transition. Panel d: normalized χ^2 of the Weeds fit as a function of the excitation temperature. Panel e: best Weeds fit to the (1,1) transition corresponding to an excitation temperature of 8 K. Panels f–m: spectra of other transitions included in the analysis. Green lines correspond to a single-component Gaussian fit and 3σ upper limits to CCS, C_3S, and c-C_3HD.

temperature calibration. A relative gain correction was applied to the data to account for antenna deformations as a function of elevation.

The beam efficiency was not measured directly during our observations. To convert the observed spectral intensities to the main beam brightness temperature units, we used the main beam efficiency of η_{mb} = 50% (Pineda et al. 2019; Lis et al. 2025) rather than the measured DSN aperture efficiency of η_A = 35.5%. This choice is justified given the expected extent of the molecular emission. Moreover, the absolute intensity calibration is not critical, as opacity effects are small or moderate for all detected lines except for ammonia. We also used only the relative abundance ratios among the molecules rather than absolute abundances with respect to H_2 in the comparison with TMC-1.

Subsequent data reduction was carried out using the Institut de radioastronomie millimétrique (IRAM) CLASS data reduction software[3]. The data reduction included blanking of noisy channels near the band edges and removing linear baselines from individual scans fit in the vicinity of each line of interest. The resulting baseline-removed spectra were then averaged with $1/\sigma^2$ weighting to produce the final spectra used in the analysis.

The resulting spectra of HOPS-108 are shown in Fig. 1, as an example. Molecules included in our analysis are NH_3, c-C_3H_2, HC_3N, HC_5N, CCS, C_3S, and c-C_3HD. Given the variations in the observing time among sources and the intrinsic line strengths, not all lines are detected in all sources. In cases of non-detections, we report 3σ upper limits based on the noise measured in the spectra at the corresponding line frequencies. In the case of HOPS-108, upper limits are determined for CCS, C_3S, and c-C_3HD (Figs. 1j–1l). Spectra of the remaining sources are shown in the appendix.

3. Results

Using the spectral fits to the DSS-43 spectra, we first derived the gas kinetic and excitation temperatures and estimated H_2 densities based on observations of ammonia inversion lines. We then determined molecular column densities using the Weeds modeling package[4], which can perform simple modeling of the observed spectra under the assumption of local thermodynamic equilibrium (LTE). The LTE approximation is justified as collisional cross sections are not available for some of the species considered here.

3.1. Gas temperatures

Calculations of molecular column densities require prior knowledge of the excitation temperature (via LTE calculations) or kinetic temperature and density – via radiative transfer models such as the large velocity gradient (LVG) approach. The kinetic temperature can be estimated from observations of the ammonia inversion lines (see Appendix B of Lis et al. 2025). The ammonia (1,1) to (3,3) inversion lines are detected with high signal-to-noise ratio in all sources. In all sources, the (1,1) and (2,2) lines are characterized by narrow line widths, with the hyperfine structure clearly detected (Figs. 1a and 1b). However, the (3,3) line in some sources shows an additional broader component originating in the outflow driven by an embedded protostellar source (see Fig. 1c for an example). The broad component is most prominent in the (3,3) line, as this high-energy transition is only weakly excited in the cold gas responsible for the narrow component emission. In such cases, we fitted the line profile with two Gaussian components to separate the narrow-line emission for temperature determination.

The resulting estimates of the kinetic temperature for all DSS-43 targets based on the observed line intensities of the ammonia inversion lines are listed in Table 2. They are in agreement with the values reported by Wienen et al. (2018).

To determine the ammonia excitation temperature, we performed least-squares fits to the ammonia (1,1) spectra for different excitation temperatures with the ammonia column density, line center velocity, and line width as free parameters. The source size was fixed at the value derived from the SPIRE 350 μm observations. Figure 1d shows the normalized χ^2 as a function of the excitation temperature for HOPS-108. The minimum is reached for T_{ex} = 8 K, as compared to the kinetic temperature of 19.6 K. The Weeds best fit to the ammonia (1,1) spectrum for this excitation temperature is shown as the green line in Fig. 1e, with the residuals shown below. Fits for other sources are shown in the appendix.The resulting ammonia excitation temperatures for all DSS-43 targets are listed in Table 2.

Although the fitting procedure used here for the determination of the ammonia excitation temperature is different from the simple hyperfine structure fit used by Lis et al. (2025), we

[3] https://www.iram.fr/IRAMFR/GILDAS/

[4] https://www.iram.fr/IRAMFR/GILDAS/doc/html/weeds-html/weeds.html

Table 2. Source sizes, temperatures, and molecular column densities.

Source	Size	T_k	T_{ex}	NH_3	c-C_3H_2	HC_3N	HC_5N	CCS	C_3S	c-C_3HD
HOPS-108	58	19.6	8.0	1.36(15)	1.05(13)	9.71(12)	1.95(12)	5.27(12)[a]	3.57(11)[a]	8.19(11)[a]
HOPS-373	50	14.9	7.0	6.63(14)	8.88(12)	1.00(12)[a]	2.56(11)[a]	1.13(12)	4.22(11)[a]	1.12(12)[a]
Vela C IRS 31 14	41	15.1	6.0	2.49(15)	1.83(13)	6.60(12)	1.57(12)	3.77(12)	7.93(11)	1.38(12)[a]
BHR71-IRS1	24	13.1	10.0	1.77(15)	1.22(14)	3.81(13)	7.90(12)	9.78212)	7.54(12)[b]	1.31(13)[a]
G300.91+0.88	68	14.7	4.5	*1.76(16)*	2.21(13)	8.15(12)	1.52(12)	4.49(12)	1.46(12)	7.95(11)[a]
G304.76+1.34	109	13.7	4.3	*1.40(16)*	1.73(13)	4.80(12)	1.26(12)	3.99(12)	9.71(11)	1.09(12)[a]
G309.91+0.32	66	17.6	5.2	*9.82(15)*	1.29(13)	7.34(12)	1.53(12)	2.72(12)	9.70(11)[a]	2.08(12)
G300.91+0.88	68	14.7	7.0	2.13(15)	2.01(13)	7.53(12)	1.12(12)	4.70(12)	1.22(12)	8.08(11)[a]
G304.76+1.34	109	13.7	7.0	1.32(15)	1.56(13)	3.06(12)	7.98(11)	4.04(12)	7.71(11)	1.07(12)[a]
G309.91+0.32	66	17.6	7.0	2.86(15)	1.35(13)	7.34(12)	1.35(12)	3.00(12)	9.11(11)[a]	2.23(12)

Notes. Entries in the table are source, source size (arcsec), kinetic and excitation temperatures (K), and molecular column densities (cm^{-2}, with the value in parentheses being the exponent). [(a)]3σ upper limit. [(b)]Given the difference in the center velocity and line width compared to CCS, we consider this an upper limit. The bottom three lines show revised column densities G300.91+0.88, G304.76+1.34, and G309.91+0.32 assuming an excitation temperature of 7.0 K, as described in the text.

confirmed that it gives consistent results for the Chamaeleon cores. In the case of Cha-C2, we derived the same excitation temperature of 5.5 K using the method presented here, while for Cha-MMS1, our best-fit excitation temperature using Weeds is 7.0 K, compared to the 7.6 K in Lis et al. (2025). We note that the ammonia column density is sensitive to T_{ex} at low excitation temperatures (see the red line in Fig. 1d). In the case of Cha-MMS1, lowering the excitation temperature from 7.6 to 7 K increases the column density by ~25%.

3.2. Gas densities

Since collisional rate coefficients are available for ammonia, the combination of the kinetic and excitation temperature can be used to estimate the H_2 density using LVG models. We used the offline version of the RADEX code (van der Tak et al. 2007) to calculate the ammonia excitation temperature as a function of density for a given kinetic temperature. Several sets of collisional cross sections with $o-$ and $p-H_2$ are available in the literature (Danby et al. 1988; Demes et al. 2023; Loreau et al. 2023). The Demes et al. (2023) calculations are for collisions with both $o-$ and $p-H_2$. The Danby et al. (1988) and Loreau et al. (2023) cross sections are only for collisions with $p-H_2$. However, the Loreau et al. (2023) calculations resolve the NH_3 hyperfine structure.

Figure 2 (top panel) shows the excitation temperature of the NH_3 (1,1) line (the strongest hyperfine-structure, HFS, component in the case of Loreau et al. 2023 cross sections) in HOPS-108 as a function of the gas density. The calculations assume a kinetic temperature of 19.6 K, as determined above, a full width at half maximum line width of 1.3 km s^{-1}, and an NH_3 column density of 1.5×10^{14} cm^{-2}, which approximately reproduces the observed intensity of the main HFS component with the Loreau et al. (2023) cross sections[5]. The color curves correspond to different collisional cross sections. The three sets of collisional cross sections with p-H_2 (cyan, blue, and magenta) are in good agreement. For a given density, collisions with o-H_2 result in a higher excitation temperature, as $o-H_2$ is more efficient at collisional excitation than $p-H_2$. The excitation temperature of 8 K derived for HOPS-108 from the Weeds models (T_{ex}/T_k = 0.41) corresponds to a range of densities of 3.5×10^3–1.1×10^4 cm^{-3}, depending on the collisional cross-section set used.

We carried out similar calculations for BHR71-IRS1 (Fig. 2, middle panel), which has the highest T_{ex}/T_k = 0.76 in our sample, assuming a column density of 8.0×10^{13} cm^{-2}. The resulting density range is 1.7×10^4–5.0×10^4 cm^{-3}. G309.91+0.32 (Fig. 2, bottom panel) is characterized by one of the lowest T_{ex}/T_k = 0.30 in our sample. In this case, assuming an NH_3 column density of 3.8×10^{14} cm^{-2}, the resulting density range is 1.1×10^3–4.0×10^3 cm^{-3}.

In general, the most distant sources have lower volume densities, as the emission in the DSS-43 beam is dominated by extended, lower-density envelopes. BHR71-IRS1, being the closest source and relatively isolated, has the highest volume density. These calculations are not meant to provide accurate density estimates in our target sources, but instead to constrain a relevant density range for the chemical models. Based on the ratio of the excitation to kinetic temperature, we expect Cha-MMS1 to have similar density to BHR71-IRS1. Vela C IRS 21 14, HOPS-373, and Cha-C2 should be similar to HOPS-108, while G300.91+0.88 and G304.76+1.34 should be similar to G309.01+0.32. We note that the densities reported here are average values in the relatively large DSS-43 beam. *Herschel* dust continuum images indicate the presence of compact sources, which will be characterized by higher densities.

3.3. Local thermodynamic equilibrium molecular column densities

Since collisional rates are not available for many of the molecules studied here, we consistently used the LTE approach as implemented in the Weeds software package. We used molecular spectroscopy data from the CDMS catalog (Müller et al. 2001, 2005) in the calculations. We assumed the same excitation temperature for all molecules equal to the ammonia excitation temperature. More details on the Weeds modeling can be found in Lis et al. (2025). For HC_3N, the hyperfine structure is not included in Weeds. Moreover, while the satellite components are detected in HOPS-108 (Fig. 1m), only the two strongest, blended central components are detected in most sources. Since the emission is optically thin, we performed a Gaussian fit to the two

[5] Note that the column densities used in the LVG calculations are averaged values in the DSN beam, while those reported in Table 2 are peak values in a pencil beam.

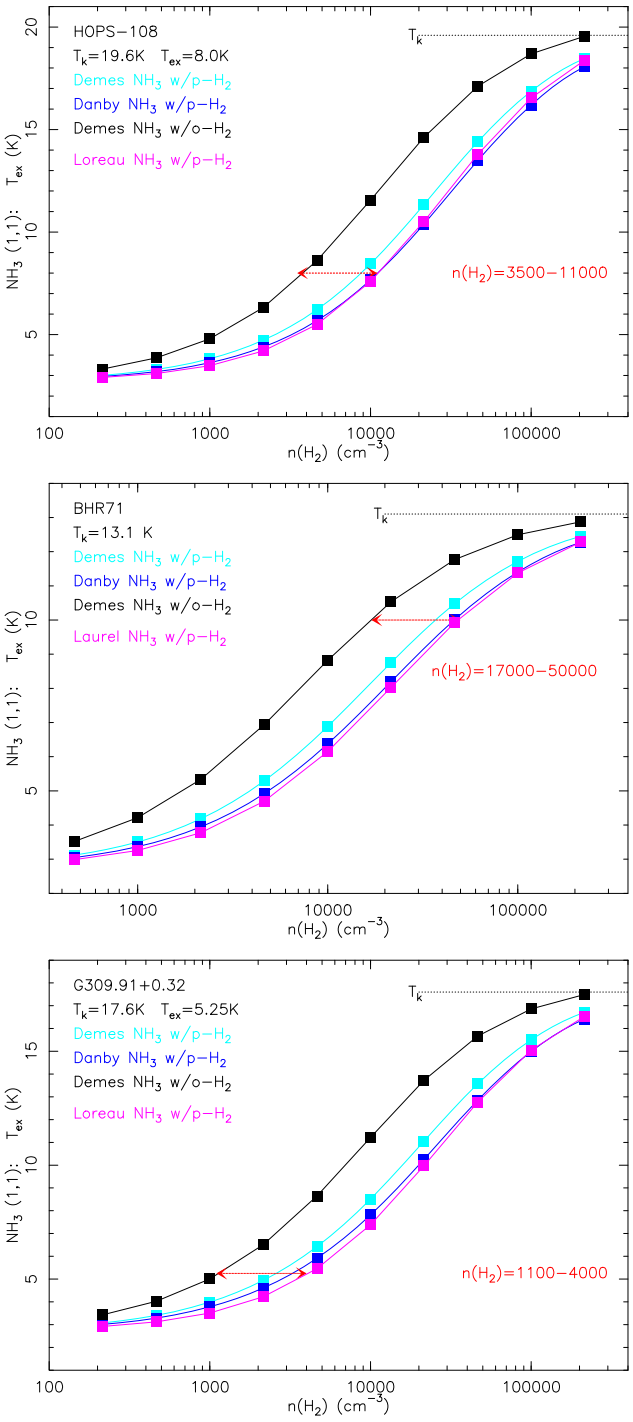

Fig. 2. LVG models of the NH_3 (1,1) excitation in (from top to bottom): HOPS-108, BHR71-IRS1, and G309.91+0.32. The color curves correspond to different collisional cross sections, as described in the legend.

strongest, blended HFS components and multiplied the column density by 1.395 to correct for the weak satellite components.

The resulting molecular column densities are listed in Table 2. These should be interpreted as peak column densities in a pencil beam, as the convolution of the source size with the telescope beam is carried out directly in Weeds. The deuterated species c-C_3HD is not detected in any of the sources studied here. The only molecules detected in HOPS–373 are ammonia and C_3H_2. Sulfur bearing species CCS and C_3S are not detected in HOPS–108.

Table 3 gives selected column density ratios based on column densities reported in Table 2. Values for the two Chamaeleon sources and TMC-1 are from Lis et al. (2025). The c-C_3H_2/HC_5N, HC_3N/HC_5N, and CCS/C_3S ratios are in general comparable to the values derived in the Chamaeleon cores. However, the c-C_3HD/c-C_3H_2 upper limits are a factor of 2–3 lower than in Chamaeleon.

HC_5N has three rotational transitions within the DSS-43 frequency range, with similar upper level energies and excitation requirements. A comparison of the observed line intensities with the best-fit Weeds models for the individual lines show that the uncertainties in the molecular column densities, including calibration and modeling, are in the range 3% (HOPS-108) up to ~50% (BHR71-IRS1, G300.91+0.88, G304.76+1.34). We estimate the overall uncertainties of the column density ratios reported in Table 3 to be a factor of 2–3.

3.4. High ammonia column densities in G300.91+0.88, G304.76+1.34, and G309.91+0.32

One striking result of the calculations presented above are the very high ammonia column densities in G300.91+0.88, G304.76+1.34, and G309.91+0.32, about an order of magnitude higher than those in Chamaeleon or other sources in our sample. These targets were selected from the deuterated ammonia survey of Wienen et al. (2021) and, therefore, are naturally strong ammonia emitters. However, the high column densities derived from the Weeds LTE fits require further investigation. The kinetic temperatures of these three sources, 14–18 K, are in the same range as those derived for other sources, 13–20 K. However, their ammonia excitation temperatures are very low, 4.1–5.2 K, compared to 6–10 K in other sources. This is understandable, as these sources are more distant (Table 1); the DSS-43 beam thus primarily probes their lower-density, extended envelopes. The resulting $T_{ex}/T_k \sim 0.3$ is low, compared to 0.4–0.76 in other sources. The high column densities are a direct consequence of the low excitation temperatures, as the column density is a strong function of the excitation temperature in the low temperature regime (see the red curves in panel d in Figs. A.4–A.6).

The source sizes used in the Weeds fits were derived from the *Herschel*/SPIRE 350 μm dust continuum images. In particular, G304.76+1.34 has the largest source size in our sample, 109″, much larger than the DSS-43 beam. To investigate the dependence of the NH_3 column on the assumed source size, we carried out additional Weeds fits for this source assuming smaller source sizes of 60″ (a typical value for other sources) and 41″ (the low Vela C IRS 31 41 value). The best fit for the source size of 60″ results in an excitation temperature of 5.0 K and an NH_3 column density of 8.1×10^{15} cm^{-2}, a factor of 1.7 times lower than the value reported in Table 2. The best fit for the source size of 41″ results in an excitation temperature of 5.5 K and the same NH_3 column density 8.1×10^{15} cm^{-2}.

For G300.91+0.32, decreasing the source sizes to 41″ increases the excitation temperature to 5.3 K and decreases the NH_3 column density to 1.25×10^{16} cm^{-2}, a factor of 1.4 lower than the value reported in Table 2. For G309.91+0.32, decreasing the source sizes to 41″ increases the excitation temperature to 6.5 K and decreases the NH_3 column density to 6.7×10^{15} cm^{-2}, a factor of 1.5 lower than the value reported in Table 2. We thus conclude that the assumed source size has only a moderate effect on the resulting NH_3 column densities and cannot explain the difference between G300.91+0.88, G304.76+1.34, and G309.91+0.32 and the other sources in our sample.

Table 3. Molecular column density ratios.

Source	NH_3/HC_5N	$NH_3/c\text{-}C_3H_2$	$c\text{-}C_3H_2/HC_5N$	$c\text{-}C_3HD/c\text{-}C_3H_2$	HC_3N/HC_5N	CCS/HC_5N	CCS/C_3S
HOPS–108	700	130	5.4	0.08[a]	5.0	0.27[a]	–
HOPS–373	–	75	–	0.13[a]	–	–	–
Vela C IRS 31 14	1600	140	12	0.08[a]	4.2	2.4	4.8
BHR71–IRS1	220	15	15	0.11[a]	4.8	1.2	1.3
G300.91+0.88	*12 000*	*830*	14	0.04[a]	5.4	3.0	3.1
G304.76+1.34	*11 000*	*810*	14	0.06[a]	4.0	3.2	4.1
G309.91+0.32	*6200*	*760*	8.2	0.16[a]	4.6	1.8	2.9
Cha MMS1	1000	120	8.3	0.22	4.6	3.8	5.6
Cha C2	1200	170	7.1	0.24	3.7	6.8	5.4
TMC-1	8.5	26	0.32	0.28	3.9	1.7	7.1
G300.91+0.88	1890	105	18	0.04[a]	6.7	4.2	3.9
G304.76+1.34	1650	85	20	0.07[a]	5.6	5.1	5.2
G309.91+0.32	1210	210	10	0.17[a]	5.7	2.3	3.3

Notes. Entries in the table are source and selected molecular column density ratios based on column densities reported in Table 2. [a]3σ upper limit. Chamaeleon and TMC-1 values are from Lis et al. (2025). The bottom three lines show revised column density ratios for G300.91+0.88, G304.76+1.34, and G309.91+0.32 assuming a higher excitation temperature of 7.0 K, as described in the text.

Given the difference in the opacity of the main NH_3 (1,1) hyperfine component and the satellite components, the lines may not trace the same gas along the line of sight. The optically thick central component traces preferentially the surface of the cloud, while the weaker optically thin satellite components trace all gas along the line of sight. Our fitting approach assumes a single excitation temperature. In reality, density and temperature gradients are likely to exist, resulting in variations of the excitation temperature along the line of sight, depending on the presence or absence of a central heating source. We note that high-velocity emission is detected in the NH_3 (3,3) spectra of G300.91+0.88 and G309.91+0.32, suggesting the presence of embedded sources, which may heat up the central parts of these cores. However, the NH_3 (3,3) line in G304.76+1.34 only shows a narrow component, suggesting absence of a central source. These three sources thus likely have different temperature profiles. Yet, despite these differences, they are all characterized by low excitation temperatures and high NH_3 column densities.

To further quantify the sensitivity of the NH_3 column density to the assumed excitation temperature, we fitted the NH_3 (1,1) spectra in G300.91+0.88, G304.76+1.34, and G309.91+0.32 assuming an excitation temperature of 7 K, an average value for the remaining sources, including the two Chamaeleon cores. The resulting NH_3 column densities are reduced by large factors of 8.2, 11, and 3.4, respectively. The revised column densities for all molecules are reported in the bottom three lines of Table 2. The corresponding revised abundance ratios are listed in the bottom three lines of Table 3 and are used for comparison with the chemical models.

Detailed radiative transfer models would be required to better constrain the physical conditions and molecular column densities. This would also require additional higher spatial resolution mapping observations and is beyond the scope of the present paper.

4. Chemical modeling

The state-of-the-art gas–grain astrochemical model DNAUTILUS, originally introduced by Majumdar et al. (2017a), was employed to compute the chemical composition of the observed dense cores using observationally constrained densities and temperatures. Since its initial implementation, the model has undergone substantial development, with successive updates to the chemical network presented in a series of next-generation DNAUTILUS studies spanning multiple evolutionary stages of star-forming environments. These include starless cores (Tasa-Chaveli et al. 2025), low-mass star-forming regions (Majumdar et al. 2017b), high-mass star-forming regions (Li et al. 2025), and protoplanetary disks (Kashyap et al. 2024), among others.

DNAUTILUS is specifically designed to model deuterium fractionation, including multiple deuterated isotopologs, within both two-phase (gas and grain surface) and three-phase (gas, grain surface, and grain bulk mantle) frameworks. The current network includes 1606 gas-phase species, 834 grain-surface species, and 737 grain-mantle species, connected through 83 715 gas-phase reactions, 10 967 surface reactions, and 9431 mantle reactions. Table A.1 lists the dominant formation and destruction process for the molecules studied here for the best-fit model. The model solves the time-dependent chemical evolution of molecular abundances in both two-phase mode, where the grain is treated as chemically homogeneous, and three-phase mode, where the grain surface and bulk mantle are treated as chemically distinct reservoirs.

The chemical network incorporates 15 elements, with initial elemental abundances listed in Table 1 of Majumdar et al. (2017a). Molecular hydrogen is initially present as H_2 and HD, while all other elements are assumed to be in atomic form. Elements with ionization potentials below 13.6 eV (C, S, Si, Fe, Na, Mg, Cl, and P) are initially assumed to be singly ionized. The elemental abundance of carbon is kept fixed across all models, while four C/O ratios (0.5, 0.7, 0.9, and 1.4) are explored by varying the elemental oxygen abundance.

All simulations were performed using the three-phase version of DNAUTILUS. The cosmic-ray ionization rate was fixed at 1.3×10^{-17} s^{-1}. The ranges of densities and temperatures adopted for each core are listed in Table 4 and are based on the observationally derived values reported in Table 2. In most models, the gas and dust temperatures are assumed to be equal. The only exceptions are the Chamaeleon cores, which are discussed separately below.

Table 4. Parameters used for the chemical models of each core.

Source	n	T_{gas}	T_{grain}
HOPS-108	2×10^3–1×10^4	19.6	19.6
Vela C IRS 31 14	2×10^3–1×10^4	15.1	15.1
BHR71-IRS1	1×10^4–5×10^4	13.1	13.1
G300.91+0.88	2×10^3–1×10^4	14.7	14.7
G304.76+1.34	2×10^3–1×10^4	13.7	13.7
G309.91+0.32	2×10^3–1×10^4	17.6	17.6
Cha MMS1 (high n)	3×10^5–1.4×10^6	8.5–11	13.2
Cha MMS1 (low n)	1×10^4–5×10^4	11.0	13.2
Cha C2 (high n)	2×10^5–8×10^5	8.5–11	13
Cha C2 (low n)	3×10^3–1×10^4	11.0	13.0
TMC-1	3×10^4	10.0	10.0

Notes. Entries in the table are the source, density (cm^{-3}), gas and grain temperatures (K). C/O ratios for each set of parameters are set to 0.5, 0.7, 0.9 and 1.4.

Table 5. Best-fit model parameters for each core.

Source	C/O	n	T_{gas}	t
HOPS-108	0.7	8×10^3	19.6	8.0×10^5
Vela C IRS 31 14	0.5	2×10^3	15.1	5.0×10^6
BHR71-IRS1	0.7	1×10^4	13.1	6.3×10^5
G300.9+0.88	0.7	2×10^3	14.7	2.5×10^6
G304.76+1.34	0.5	2×10^3	13.7	5.0×10^6
G309.91+0.32	0.7	1×10^4	17.6	6.3×10^5
Cha MMS1 (high n)	0.7	3×10^5	10.0	6.3×10^4
Cha MMS1 (low n)	0.7	2×10^4	11.0	6.3×10^5
Cha C2 (high n)	0.5	2×10^5	8.5	8.0×10^4
Cha C2 (low n)	0.5	8×10^3	11.0	1.0×10^6
TMC-1	1.4	3×10^4	10.0	6.3×10^5

Notes. Entries in the table are the source, C/O ratio, density (cm^{-3}), gas temperature (K), and time (yr). The best-fit models are determined by the minimum value of the distance of disagreement (D) parameter (Eq. (1)).

For Cha C2 and Cha MMS1, the densities derived from the NH_3 emission in this paper are 3.5×10^3–1.1×10^4 cm^{-3} and 1.7×10^4–5×10^4 cm^{-3}, respectively. These are lower than reported in Lis et al. (2025) where the 350 μm emission from *Herschel*/SPIRE in a smaller beam was used to determine densities of 2–8×10^5 cm^{-3} for Cha C2 and 3–14×10^5 cm^{-3} for Cha MMS1. The H_2 densities depend on the tracer (e.g., molecular tracers with different critical densities trace different regions of the core), and parameters used to convert the dust optical depth into the column density. Some of the parameters, for example the grain emissivity coefficient, are very uncertain, leading to uncertainties in the number density. We therefore considered two sets of models, one that uses the ammonia densities derived here, which are representative of the cloud envelope, and another one that uses the higher densities (and temperatures) from Lis et al. (2025), characteristic of the denser gas at the center. They are denoted "low n" and "high n", respectively, in Table 4. Both sets of models assume a grain temperature (T_d) of 13.2 K for MMS1 and 13 K for C2.

The best-fit model was determined by calculating the distance of disagreement (Wakelam et al. 2024, 2010):

$$D(t) = \frac{1}{N_i}\Sigma|log(X_{mod,i}(t)) - log(X_{obs,i})|, \quad (1)$$

where N_i is the number of observations, $X_{mod,i}(t)$ is the modeled abundance as a function of time, and $X_{obs,i}$ is the observed abundance. The best-fit model has the lowest $D(t)$ and is listed in Table 5. We compared the ratios presented in Table 3 for $X_{obs,i}$ to the modeled ratios. The parameters of the best-fit models, as determined by the D parameter, are listed in Table 5.

Most cores have similar properties with densities from 2×10^3 to 2×10^4 cm^{-3} and C/O ratios of 0.5 or 0.7. The exception is TMC-1, which has a very high C/O ratio of 1.4. The chemical ages determined for each core are also similar and fall between 0.6 and 5 Myr. The oldest chemical age was found for G304.76+1.34, while the youngest were BHR71-IRS1, G309.91+0.32, and Cha2 MMS1. The less dense cores tend to be the ones with the oldest chemical age, as might be expected given that chemical timescales scale with density.

Direct comparisons of the chemical ages and elemental C/O ratios derived for the majority of the dense cores in this work with previous studies remain limited, primarily because detailed gas-grain chemical modeling is available only for a small number of well-studied sources, most notably TMC-1 (e.g., Majumdar et al. 2017a; Navarro-Almaida et al. 2021; Tasa-Chaveli et al. 2025). Previous kinetic models of TMC-1 generally infer chemical ages of order 0.1−6 Myr, depending on the adopted chemical network, elemental abundances, and physical conditions (e.g., Majumdar et al. 2017a; Navarro-Almaida et al. 2021; Wakelam et al. 2024; Maitrey et al. 2025). Our derived chemical ages of ∼0.6–5 Myr are broadly consistent with the range expected for cold dense cores, particularly considering that chemical timescales scale with density (Agúndez & Wakelam 2013).

The C/O ratios inferred for most of the sources in our sample (0.5–0.7) are also consistent with the elemental abundances commonly adopted in dense cloud chemical models based on diffuse cloud depletion studies toward ζ Oph (Jenkins 2009; Hincelin et al. 2011). The higher C/O ratio derived for TMC-1 in our modeling is also consistent with previous studies of this source, showing that enhanced C/O ($\gtrsim$1) increases the production of long carbon-chain molecules and cyanopolyynes toward the cyanopolyyne peak (Loomis et al. 2021; Burkhardt et al. 2021; Byrne et al. 2026). The sensitivity of modeled abundances to the adopted C/O ratio has long been recognized in dense-core chemical models, particularly for TMC-1, where proposed elemental C/O ratios span a wide range from ∼0.55 to ∼1.4 (Agúndez & Wakelam 2013). However, detailed chemical modeling studies for other dense cores observed in our survey remain scarce. Therefore, the chemical ages derived here provide useful additional constraints on the evolutionary stages of such dense cores. It should also be noted that inferred chemical ages depend on assumptions regarding the adopted chemical network, initial elemental abundances, and chemical desorption processes, which can shift the best-fit times by factors of a few (Wakelam et al. 2024; Maitrey et al. 2025).

Figure 3 compares the observed molecular abundance ratios with those predicted by our best-fit models, expressed as the ratio of observed to modeled values. For most species, the agreement is within a factor of 10. A notable exception is the CCS/HC_3N ratio, for which the model underpredicts the observed ratio. This discrepancy likely reflects a combination of the longstanding "sulfur depletion" problem in astrochemistry (Majumdar et al. 2016; Vidal et al. 2017) and limitations in reproducing

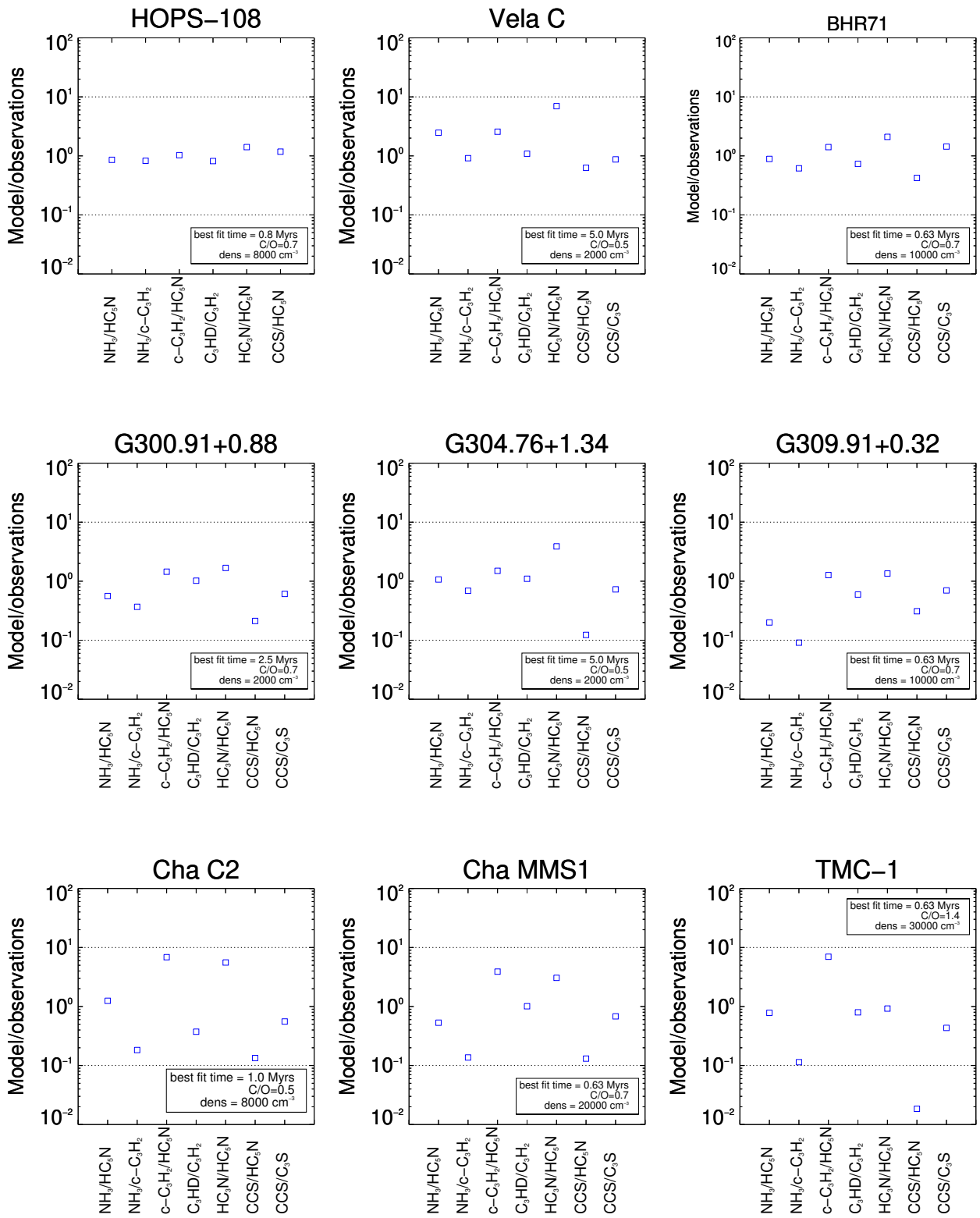

Fig. 3. Models ratios/observed ratios for best-fit model for each core. The horizontal dashed lines show ratios of 10 and 0.1. Cha C2 and MMS1 models assume the "low n" conditions derived in this study.

early-time carbon-chain chemistry. Adopting an elemental sulfur abundance significantly below its cosmic value (a few $\times 10^{-5}$; Jenkins 2009) is commonly required in dense-cloud models to avoid overproducing the observed S-bearing species (Majumdar et al. 2016; Vidal et al. 2017). In this work, we adopted a depleted sulfur abundance of 8×10^{-8}, a value commonly used in dense core chemical models (Majumdar et al. 2016; Majumdar et al. 2017a; Navarro-Almaida et al. 2021; Wakelam et al. 2024; Maitrey et al. 2025). This may suppress the formation efficiency of sulfur-bearing carbon chains such as CCS. Seo et al. (2019) demonstrated the strong sensitivity of the CCS abundance on the assumed initial sulfur abundance in dense cores of TMC-1.

In addition, different degrees of sulfur depletion may be present across dense cores (Seo et al. 2019; Vastel et al. 2018).

In practice, a too-low modeled CCS/HC_3N ratio indicates either an underproduction of CCS or an overproduction of HC_3N under the adopted physical and chemical conditions. Since CCS is directly sensitive to the available gas-phase sulfur reservoir, whereas HC_3N primarily traces carbon- and nitrogen-chain chemistry, enhanced sulfur depletion preferentially reduces CCS, thereby lowering the CCS/HC_3N ratio. In addition, the balance between carbon-chain growth and oxidation pathways, regulated by the elemental C/O ratio, plays a key role in controlling the relative abundances of CCS and HC_3N.

Moreover, the use of a single-point physical model may not adequately capture the spatial differentiation between CCS- and HC_3N-emitting regions. CCS is expected to preferentially trace relatively diffuse and chemically younger layers, while HC_3N is more likely to arise from denser and better-shielded gas. Such chemical and physical stratification can further contribute to the observed discrepancy.

Future work incorporating more realistic physical structures and systematically exploring a range of initial sulfur abundances, spanning different degrees of depletion, will be essential to reconcile the modeled and observed CCS/HC_3N ratios.

5. Summary

With this work we have extended our 1.3 cm wavelength radio survey for organics in the southern hemisphere by observing seven dense cores selected from the ALMA COMPASS program (HOPS-108, HOPS-373, and BHR-71) and the deuterated ammonia survey of Wienen et al. (2021, G300.91+0.88, G304.76+1.34, and G309.91+0.32) using the 70 m DSS-43 antenna of NASA's DSN. Prior observations of two Chamaeleon cores, MMS1 and C2 (Lis et al. 2025), are also included in the analysis.

The main results can be summarized as follows:

- Observations of the NH_3 (1,1) inversion line were used to determine the excitation temperatures and the average gas kinetic temperatures, which vary between ∼11 and 20 K.
- LVG models of the NH_3 (1,1) inversion line were then used to determine the average H_2 densities. The results are sensitive to the collisional cross sections used, and vary among sources from $(1-5) \times 10^4$ cm^{-3} in BHR-71 to $(2-10) \times 10^3$ cm^{-3} in the more distant sources from the deuterated ammonia sample.
- Molecular column densities (and upper limits) of NH_3, *c*-C_3H_2, HC_3N, HC_5N, CCS, C_3S, and *c*-C_3HD were derived for each source under the assumption of LTE. The resulting column density ratios were compared with predictions of the state-of-the-art gas–grain astrochemical model DNAUTILUS (Majumdar et al. 2017a). These comparisons were used to constrain the elemental C/O ratio and the chemical age of each source.
- Most cores show similar C/O ratios in the range 0.5−0.7, significantly lower than the well-studied carbon-chain-rich dense core TMC-1, which is characterized by C/O ∼1.4 and enhanced hydrocarbon chemistry.
- The inferred chemical ages span ∼0.6−5 Myr. The oldest chemical age is found for G304.76+1.34, while BHR71-IRS1, G309.91+0.32, and Cha2 MMS1 are chemically the youngest.

Our results showcase the synergistic approach of combining radio observations using the DSS-43 antenna with state-of-the-art astrochemical models to study the chemical composition of southern hemisphere dense cores, as a complement to Green Bank Telescope observations of northern sources.

Acknowledgements. This research was carried out at the Jet Propulsion Laboratory, California Institute of Technology, under a contract with the National Aeronautics and Space Administration (80NM0018D0004) and funded through the internal Research and Technology Development program. We thank Steve Lichten, Joe Lazio, and the DSN staff for their support and assistance with the DSS-43 observations. L.M. acknowledges funding support from the DAE through the NISER project RNI 4011.

References

Agúndez, M., & Wakelam, V. 2013, Chem. Rev., 113, 12, 8710
Bergin, E. A., Hirschmann, M. M., & Izidoro, A. 2026, arXiv e-prints [arXiv:2602.10308]
Burkhardt, A. M., Loomis, R. A., Shingledecker, C. N., et al. 2021, Nat. Astr., 5, 181
Byrne, A. N., Shingledecker, C. N., Bergin, E. A., et al. 2026, ApJ, 998, 95
Cernicharo, J., Agúndez, M., Cabezas, C., et al. 2021, A&A, 649, L15
Cernicharo, J., Agúndez, M., Cabezas, C., et al. 2022, EPJ Web Conf., 265, 00041
Cernicharo, J., Cabezas, C., Fuentetaja, R., et al. 2024, A&A, 690, L13
Danby, G., Flower, D. R., Valiron, P., et al. 1988, MNRAS, 235, 229
Demes, S., Lique, F., Loreau, J., & Faure, A. 2023, MNRAS, 524, 2368
Furlan, E., Fischer, W. J., Ali, B., et al. 2016, ApJS, 224, 5
Green, J. D., Evans, N. J., Jorgensen, J. K., et al. 2013, ApJ, 770, 123
Hincelin, U., Wakelam, V., Hersant, F., et al. 2011, A&A, 530, A61
Jenkins, E. B. 2009, ApJ, 700, 1299
Kashyap, P., Majumdar, L., Dutrey, A., et al. 2024, ApJ, 976, 258
Kuiper, T. B. H., Langer, W. D., & Velusamy, T., 1996, ApJ, 468, 761
Kuiper, T. B. H., Franco, M., Smith, S., et al. 2018, J. Astron. Instrum., 8, 1950014
Li, Y., Wang, J., et al. 2025, ApJ, 978, 156
Lis, D. C., et al. 2025, A&A, 696, A61
Loomis, R. A., Burkhardt, A. M., Shingledecker, C. N., et al. 2021, Nat. Astr., 5, 188
Loreau, J., Faure, A., Lique, F., et al. 2023, MNRAS, 526, 3213
McGuire, B. A., Loomis, R. A., Burkhardt, A. M., et al. 2021, Science, 371, 1265
Maitrey, S., Majumdar, L., Manilal, V., et al. 2025, A&A, 699, A332
Massi, F., Lorenzetti, D., & Giannini, T. 2003, A&A, 399, 147
Majumdar, L., Gratier, P., Vidal, T., et al. 2016, MNRAS, 458, 1859
Majumdar, L., Gratier, P., Ruaud, M. et al. 2017a, MNRAS, 466, 4470
Majumdar, L., Gratier, P., Andron, I., Wakelam, V., & Caux, E. 2017b, MNRAS, 466, 4770
McGuire, B. A., Burkhardt, A. M., Kalenskii, S., et al. 2018, Science, 359, 202
McGuire, B. A., Burkhardt, A. M., Loomis, R. A., et al. 2020, ApJ, 900, L10
Müller, H., Thorwirth, S., Roth, D. A., & Winnewisser, G. 2001, A&A, 370, L49
Müller, H., Schlöder, F., Stutzki, J., & Winnewisser, G. 404 2005, J. Mol. Struc., 742, 215
Navarro-Almaida, D., Fuente, A., Majumdar, L., et al. 2021, A&A, 653, A15
Pineda, J. L., Horiuchi, S., Anderson, L. D., et al. 2019, ApJ, 886, 1
Saul, M. 2022, MNRAS, 519, 271
Seo, Y. M., Majumdar, L., Goldsmith, P. F., et al. 2019, ApJ, 871, 134
Tasa-Chaveli, A., Fuente, A., Esplugues, G., et al. 2025, A&A, 700, A226
Tielens, A. G. G. M. 2008, ARA&A, 46, 289
Tobin, J. J., Megeath, S. T., van't Hoff, M., et al. 2019, ApJ, 886, 6
Urquhart, J. S., Konig, C., Giannetti, A., et al. 2017, MNRAS, 473, 1059
Urquhart, J. S., Figura, C., Wyrowski, F., et al. 2019, MNRAS, 484, 4444
van der Tak, F. F. S., Black, J. H., Schöier, F. L., et al. 2007, A&A 468, 627
Vastel, C., Quénard, D., Le Gal, R., et al. 2018, MNRAS, 478, 5514
Virkler, K., Kocz, J., Soriano, M., et al., 2020, ApJS, 251, 1
Vidal, T. H. G., Loison, J.-C., Jaziri, A. Y., et al. 2017, MNRAS, 469, 435
Wakelam, V., Herbst, E., & Selsis, F. 2006, A&A, 451, 551
Wakelam, V., Herbst, E., Le Borlout, J., et al. 2010, A&A, 517, A21
Wakelam, V., Gratier, P., Loison, J.-C., et al. 2024, A&A, 689, 63
Wienen, M., Wyrowski, F., Walmsley, C. M., et al. 2018, A&A, 609, A125
Wienen, M., Wyrowski, F., Walmsley, C. M., et al. 2021, A&A, 649, A21
Wenzel, G., Cooke, I. R., Changala, P. B., et al. 2024, Science, 386, 810
Wenzel, G., Speak, T. H., Changala, P. B., et al. 2025a, Nat. Astron., 9, 262
Wenzel, G., Gong, S., Xue, C., et al. 2025b, ApJ, 984, L36
Xue, C., Byrne, A. N., Morgan, L., et al. 2025, ApJS, 281, 9

Appendix A: DSS-43 spectra of the remaining sources and dominant formation and destruction processes

Figures A.1–A.6 show spectra of the remaining sources observed with DSS-43. The format is the same as in Fig. 1. The deuterated species c-C_3HD is not detected in any of the sources. In HOPS-373, only ammonia, C_3H_2, and CCS are detected. In Vela C, all lines other than c-C_3HD are detected. In BHR71-IRS1, C_3S is located in a noisy part of the spectrum. Although the feature is formally 5.4σ, owing to the difference in the central velocity and width compared to CCS, we consider it an upper limit. Weeds fits in Figs. A.4–A.6 correspond to an excitation temperature of 7 K rather than the best-fit values.

Table A.1 lists the dominant formation and destruction process for each molecule in each core.

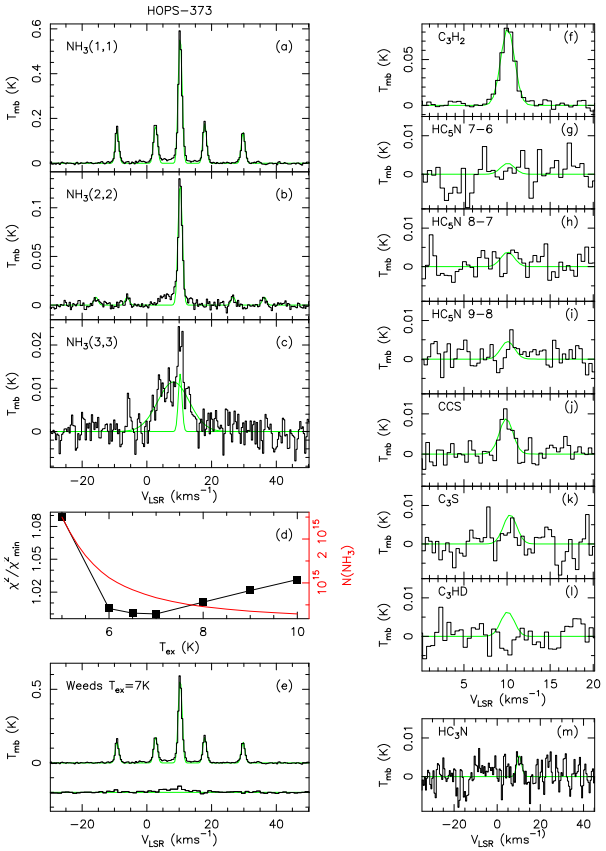

Fig. A.1. DSS-43 observations of HOPS-373.

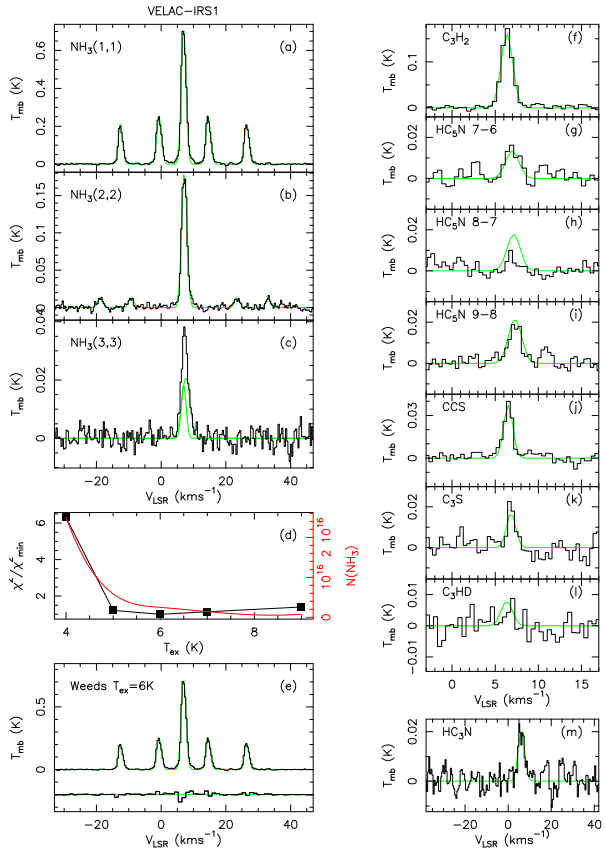

Fig. A.2. DSS-43 observations of Vela C IRS1.

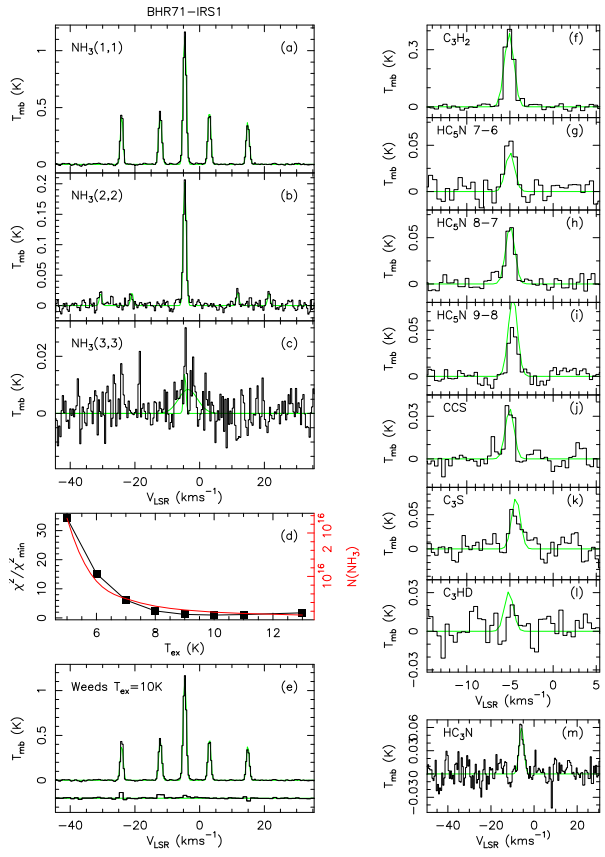

Fig. A.3. DSS-43 observations of BHR71-IRS1.

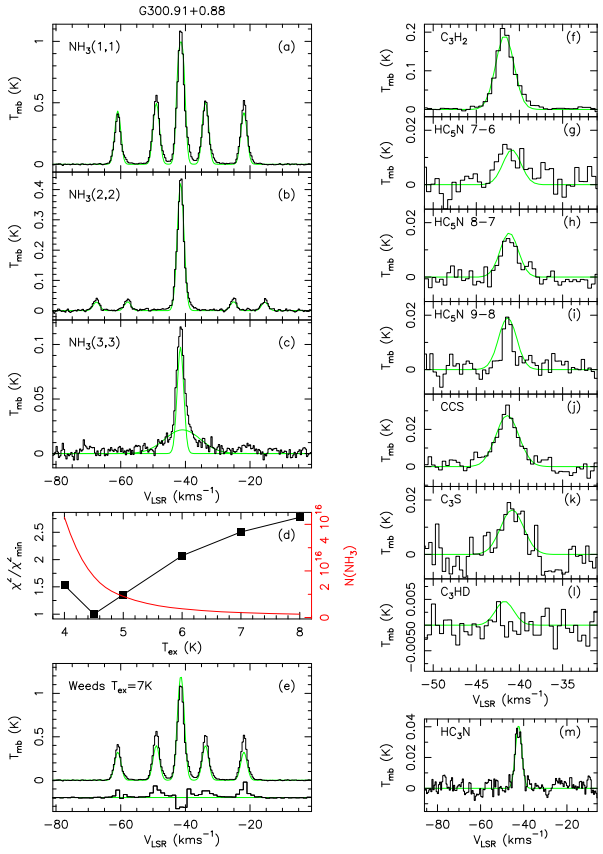

Fig. A.4. DSS-43 observations of G300.91+0.88.

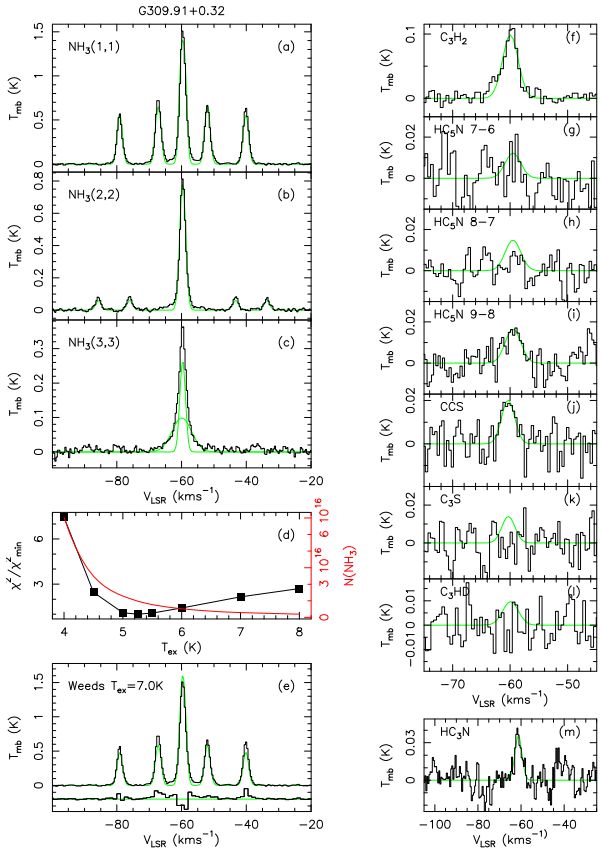

Fig. A.6. DSS-43 observations of G309.91–0.25.

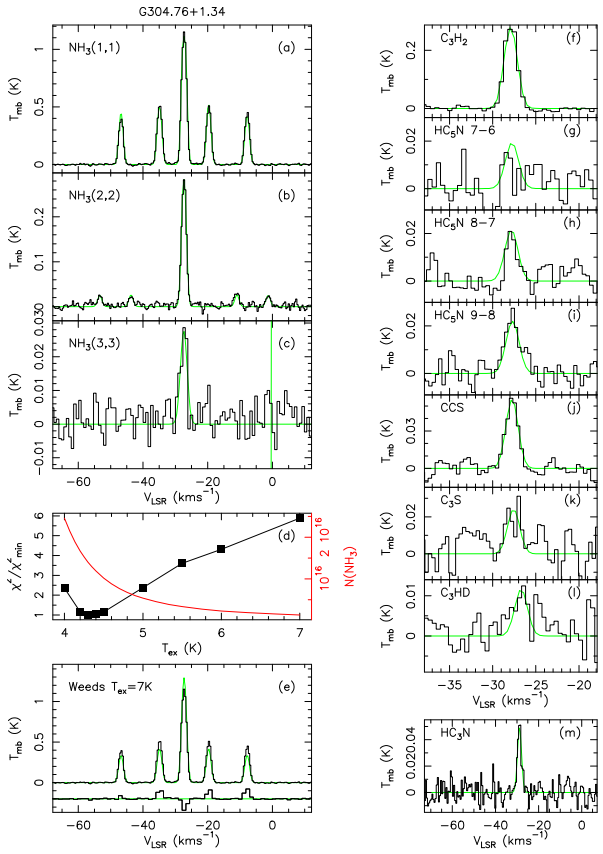

Fig. A.5. DSS-43 observations of G304.76+1.34.

Table A.1. Dominant formation and destruction processes for each molecule in each core.

Reaction	HOPS108	Vela C	BHR71	G300.9	G304.76	G309.91	Cha2 MMS1 high n	Cha2 MMS1 low n	Cha2 C2 high n	Cha2 C2 low n	TMC-1
NH_3 (production)											
$NH_4^+ + e \rightarrow NH_3 + H$	✓	✓	✓	✓	✓	✓	✓	✓	✓	✓	✓
$NH_3D^+ + \rightarrow NH_3 + D$							✓		✓		
NH_3 (destruction)											
$NH_3 + H_3^+ \rightarrow NH_4^+ + H_2$	✓	✓	✓	✓	✓	✓		✓	✓	✓	✓
$NH_3 + C^+ \rightarrow HCNH^+ + H$			✓	✓		✓					
$NH_3 + HCO^+ \rightarrow NH_4^+ + CO$			✓			✓				✓	✓
$NH_3 + H^+ \rightarrow NH_3^+ + H$			✓	✓		✓	✓	✓			
$NH_3 + H_2D^+ \rightarrow NH_3D^+ + H_2$								✓	✓		
$NH_3 + CN \rightarrow HCN + NH_2$											✓
$NH_3 + D_3^+ \rightarrow NH_2D_2^+ + HD$							✓		✓		
c-C_3H_2 (production)											
c-$C_3H_3^+ + e \rightarrow$ c-$C_3H_2 + H$	✓	✓	✓	✓	✓	✓	✓	✓	✓	✓	✓
$CH2CCH + H \rightarrow$ c-$C_3H_2 + H_2$	✓						✓		✓	✓	
$C_5H_3^+ + e \rightarrow$ c-C_3H_2 + CCH											✓
c-$C_3H_2D^+ + e \rightarrow$ c-$C_3H_2 + D$							✓		✓		
c-C_3H_2 (destruction)											
c-$C_3H_2 + H_3^+ \rightarrow$ c-$C_3H_3^+ + H_2$	✓	✓	✓	✓	✓	✓		✓	✓	✓	✓
c-$C_3H_2 + HCO^+ \rightarrow CO +$ c-$C_3H_3^+$			✓			✓				✓	✓
c-$C_3H_2 + C^+ \rightarrow C_4^+ + H_2$			✓	✓							
c-$C_3H_2 + C^+ \rightarrow C_4H^+ + H$			✓	✓							
c-$C_3H_2 + H_2D^+ \rightarrow$ c-$C_3H_2D^+ + H_2$								✓	✓		✓
c-$C_3H_2 + D_2^+ \rightarrow$ c-$C_3HD_2^+ + HD$							✓		✓		
c-$C_3H_2 + D_3^+ \rightarrow$ c-$C_3H_2D^+ + H_2$							✓				
c-C_3HD (production)											
c-$C_3H_2D^+ + e \rightarrow$ c-$C_3HD + H$	✓	✓	✓	✓	✓	✓	✓	✓	✓	✓	✓
c-$C_3HD_2^+ + e \rightarrow$ c-$C_3HD + H$							✓	✓	✓		
$C_5H_2D^+ + e \rightarrow$ c-C_3HD + CCH											✓
c-C_3HD (destruction)											
c-$C_3HD + H_3^+ \rightarrow$ c-$C_3H_2D^+ + H_2$	✓	✓	✓	✓	✓	✓		✓		✓	✓
c-$C_3HD + H_3^+ \rightarrow$ c-$C_3H_3^+ + HD$	✓	✓	✓	✓	✓	✓		✓		✓	✓
c-$C_3HD + HCO^+ \rightarrow$ c-$C_3HD^+ + CO$			✓			✓				✓	✓
c-$C_3HD + C^+ \rightarrow C_4^+ + HD$			✓	✓							
c-$C_3HD + H_2D^+ \rightarrow$ c-$C_3H_2D^+ + HD$								✓	✓		✓
c-$C_3HD + D_3^+ \rightarrow$ c-$C_3H_2D^+ + D_2$							✓		✓		
c-$C_3HD + D_3^+ \rightarrow$ c-$C_3HD_2^+ + HD$							✓		✓		

Notes. Reactions are included if they contribute more than 10% to the formation or destruction.

Table A.1. continued.

Reaction	HOPS108	Vela C	BHR71	G300.9	G304.76	G309.91	Cha2 MMS1 high n	Cha2 MMS1 low n	Cha2 C2 high n	Cha2 C2 low n	TMC-1
CCS (production)											
$HC_2S^+ + e \rightarrow CCS + H$	✓	✓	✓	✓	✓	✓	✓	✓	✓	✓	✓
$HC_3S^+ + e \rightarrow CCS + CH$	✓	✓	✓	✓	✓	✓	✓	✓	✓	✓	✓
$C_3S^+ + e \rightarrow CCS + C$	✓	✓	✓	✓	✓	✓		✓			
$DC_2S^+ + e \rightarrow CCS + D$							✓	✓	✓		
$CCH + S \rightarrow CCS + H$										✓	
$DC_3S^+ + e \rightarrow CCS + CD$							✓		✓		
CCS (destruction)											
$CCS + H_3^+ \rightarrow H_2CS^+ + H_2$	✓	✓	✓	✓	✓	✓		✓	✓	✓	✓
$CCS + O \rightarrow CS + CO$	✓		✓	✓		✓				✓	
$CCS + H^+ \rightarrow C_2S^+ + H$				✓			✓	✓			
$CCS + H_2D^+ \rightarrow HC_2S^+ + HD$								✓	✓		✓
$CCS + HCO^+ \rightarrow HC_2S^+ + CO$											✓
$CCS + D_3^+ \rightarrow DC_2S^+ + D_2$							✓		✓		
C_3S (production)											
$HC_3S^+ + e \rightarrow C_3S + H$	✓	✓	✓	✓	✓	✓	✓	✓	✓	✓	✓
$DC_3S^+ + e \rightarrow C_3S + D$							✓	✓	✓		✓
$HC_4S^+ + e \rightarrow C_3S + CH$						✓					✓
C_3S (destruction)											
$C_3S + H_3^+ \rightarrow HC_3S^+ + H_2$	✓	✓	✓	✓	✓	✓		✓	✓	✓	✓
$C_3S + H^+ \rightarrow C_3^+ + H$	✓		✓	✓	✓	✓	✓	✓			
$C_3S + HCO^+ \rightarrow HC_3S^+ + CO$			✓							✓	✓
$C_3S + C^+ \rightarrow C_4^+ + S$			✓	✓							
$C_3S + C^+ \rightarrow C_3S^+ + C$			✓	✓							
$C_3S + H_2D^+ \rightarrow HC_3S^+ + HD$								✓	✓		✓
$C_3S + D3^+ \rightarrow DC_3S^+ + D_2$							✓		✓		
HC_3N (production)											
$HC_3NH^+ + e \rightarrow HC_3N + H$	✓	✓	✓	✓	✓	✓	✓	✓	✓	✓	✓
$CN + C_2H_2 \rightarrow HC_3N + H$	✓	✓	✓	✓	✓	✓	✓	✓	✓	✓	✓
$C_3N^- + H \rightarrow HC_3N + e$	✓	✓	✓	✓	✓	✓	✓	✓	✓	✓	✓
$HC_3ND^+ + e \rightarrow HC_3N + D$							✓				
$DC_3NH^+ + e \rightarrow HC_3N + D$							✓				
HC_3N (destruction)											
$HC_3N + H_3^+ \rightarrow HC_3NH^+ + H_2$	✓	✓	✓	✓	✓	✓	✓	✓	✓	✓	✓
$HC_3N + H^+ \rightarrow HC_3N^+ + H$	✓	✓	✓	✓	✓	✓	✓	✓	✓	✓	
$HC_3N + D_3^+ \rightarrow DC_3ND^+ + HD$							✓		✓		
HC_5N (production)											
$C_4H_2 + CN \rightarrow HC_5N + H$	✓	✓	✓	✓	✓	✓	✓	✓	✓	✓	✓
$H_2C_5N^+ + e \rightarrow HC_5N + H$	✓	✓	✓	✓	✓	✓	✓	✓	✓	✓	✓
$HDC_5N^+ + e \rightarrow HC_5N + D$							✓		✓		
$C_4HD + CN \rightarrow HC_5N + D$							✓		✓		
HC_5N (destruction)											
$HC_5N + H_3^+ \rightarrow H_2C_5N^+ + H_2$	✓	✓	✓	✓	✓	✓		✓	✓	✓	✓
$HC_5N + H^+ + \rightarrow HC_5N^+ + H$	✓	✓	✓	✓	✓	✓	✓	✓			
$HC_5N + HCO^+ \rightarrow H_2C_5N^+ + CO$			✓	✓		✓	✓		✓	✓	✓
$HC_5N + D_2H^+ \rightarrow HDC_5NH^+ + HD$									✓		